JOURNAL OF MATERIALS RESEARCH AND TECHNOLOGY 2023;22:3511–3524

Available online at www.sciencedirect.com

jmr&t Journal of Materials Research and Technology

journal homepage: www.elsevier.com/locate/jmrt

Original Article

Assessment of β stabilizers additions on microstructure and properties of as-cast β Ti–Nb based alloys

Rafael Formenton dos Santos [a], *Mariana Correa Rossi* [b,*], *André Luiz Vidilli* [a], *Vicente Amigó Borrás* [c], *Conrado Ramos Moreira Afonso* [b]

[a] *Graduation Program in Materials Science and Engineering (PPG-CEM), Universidade Federal de São Carlos (UFSCar), 13.565-905, São Carlos, SP, Brazil*

[b] *Materials Engineering Department (DEMa), Universidade Federal de São Carlos (UFSCar), 13.565-905, São Carlos, SP, Brazil*

[c] *Universitat Politècnica de València, Institut de Tecnologia de Materials, Camí de Vera S/n, València, 46022, Spain*

ARTICLE INFO

Article history:
Received 18 October 2022
Accepted 22 December 2022
Available online 31 December 2022

Keywords:
Molybdenum equivalent
Surface properties
Mechanical properties
Biomedical application

ABSTRACT

The novelty of the present work lies in elucidating the correlation of Mo_{eq} with mechanical and surface parameters. The Ti–15Nb (TN-15), Ti–40Nb (TN-40), Ti–33Nb–33Zr (TNZ-33), Ti–40Nb–40Zr (TNZ40) and Ti–35Nb–7Zr–5Ta (TNZT) alloys were obtained by casting. The alloys were formed by β-Ti grains with a micrometric morphology, except the as-cast TN-15 alloy formed by α + β. Adding Nb and Zr influenced the lattice parameters of phase β, as well as the crystal structure. Grain size (GS) decreased adding Nb and Zr following this relation: TN-40 > TNZ-33>TNZT > TNZ40. The roughness decreased with rising Nb and Zr contents being in the range of 1.3–3 μm, and it was possible to correlate it with the Mo_{eq}. The contact angle and free energy surface values were inversely proportional, and the as-cast TNZ40 alloy with smaller GS was less wettable (60) than TN40 (GS: 1423 μm). The mechanical properties decreased to Mo_{eq} of 14.9 wt% then their significantly went above this value, except for the as-cast TN-15 alloy (E: 65 GPa, microhardness: 264 HV) formed mainly by a hardener phase α. Both elastic modulus and microhardness showed the same tendency as the Mo_{eq} values and the cell parameter of phase β (a_β). The oxygen content was all in accordance with ASTM E1409-13 for applications as metallic biomaterials being in the range of 0.044–0.195 wt%.

* Corresponding author.
E-mail address: mcrossi@ufscar.br (M.C. Rossi).

https://doi.org/10.1016/j.jmrt.2022.12.144

1. Introduction

The physico-chemical properties of micro- and nanostructure surfaces are critical aspects that must be investigated to acquire an effective biomaterial design strategy. Of the several surface properties, the surface energy (γs) and wettability of implant surfaces play a beneficial role in governing bone cell attachment, and can also influence electrochemical properties [1]. A growing consensus is being reached about hydrophilic surfaces with increased surface energy improving osseointegration [2,3], which means stimulating bone cells to proliferate and adhere. Extensive studies on cell adhesion responses on the surfaces of stainless steel, Ti–6Al–4V, Ta, glass, etc., prove that surface energy is proportional to cellular adhesion strength [4–6]. In another work, high-surface-energy Ti surfaces demonstrate enhanced cellular attachment in the commencing stage of the cell response by regulating the expression of cell adhesion-associated molecules [7]. Depending on the Ti alloy substrate, such as grain size (GS) and alloy elements, surface morphologies can be effectively tailored. Isomorphous elements like niobium (Nb), tantalum (Ta) and zirconium (Zr) have high solubility in titanium, and are used to improve the elastic properties of Ti alloys by lowering the β-transus temperature of Ti [8]. Moreover, properties like strength, corrosion resistance, high-temperature performance and formability can also improve elastic properties, which can become more compatible to be used as implants. It is well-known that grain boundaries (GBs) are defects with excess free energy per unit area [9]. This is evidenced by the fact that, during most thermal and chemical etching processes, the material near the GB is preferentially removed. If a solid surface is polished and then etched, the preferential removal of material near GBs reveals the interfacial lattice by demonstrating this region's great reactivity. To roughly estimate the average excess energy of a GB, the misorientation angles for different β-Ti alloys were measured. They correlated with surface and physical properties. We can imagine building the interface by first creating two free surfaces and then joining them together to form the boundary. The energy to create the two surfaces will be twice the surface energy, 2γs. However, GB energy (γ_{gb}) will be less than this because of the binding energy (B) gained when the two surfaces are brought together and new bonds are formed. The GB energy is then:

$$\gamma_{gb} = 2\gamma_s.sen\Theta - B \quad (1)$$

The anisotropic characteristics of energy have been recognized at least since the time of Smith [10]. It has been recently shown that the probability of a GB being annihilated during grain growth is related to its energy, and this leads to the anisotropic distribution of GB types [11]. Energy anisotropy arises because different GBs have distinct microscopic structures. Following the line of reasoning that leads to Eq. (1), the anisotropy in GB energy can arise from either γs or B. Macroscopically observable crystallographic parameters are used to classify boundaries with different microscopic structures. To classify boundaries, five independent parameters must be specified. Three describe the misorientation of the crystal lattice and two describe the orientation of the GB plane. The implication of having five independent parameters means that there are lots of different GB types [12]. Titanium and Ti-alloys (similar to zirconium- and Hafnium-based ones) can exist in three allotropic modifications, namely low-temperature hexagonal closely packed (hcp) α-phase, high-temperature body-centered cubic (bcc) β-phase, and hexagonal high-pressure ω-phase [13–16] and their can be designed by two different methods. These methods aim to predict the composition of the phases that will compose this β-Ti alloy. The first method is based on the stabilization of the β phase with the addition of alloying elements (β-stabilizing elements). Considering that only 10% by weight of molybdenum (Mo) is sufficient to stabilize the β phase at room temperature, it is usual to relate the percentage of betagenic element(s) with the equivalent percentage of Mo (Eq. (2)), since Mo is a powerful β-stabilizing element [17,18],

$$[Mo]_{eq} = [Mo] + [V]/1.5 + [W]/2.5 + [Nb]/3.6 + [Ta]/5 + 1,25[Cr] + 1.25[Ni] + 1.7[Mn] + 1.7[Co] + 2.5[Fe] \quad (2)$$

where the concentrations, [X], of the elements, X, are used as a percentage by weight of the alloy.

The second one is based on the parameters B_o (order/strength of the covalent bond between the titanium atom and the other alloying elements) and M_d (energy level of the d orbital), through which it is possible to predict not only the stability of the beta phase but the presence of the phases α" and ω too [16,17]. The calculus of Bo and md values are described by Eq. (3) [19,20]:

$$\overline{Bo} = \sum_i x_i (Bo)_i \quad \overline{Md} = \sum_i x_i (Md)_i \quad (3)$$

where X_i is the atomic percentage of each element i in the alloy and $(B_o)_i$ and $(M_d)_i$ are the tabulated values for element i.

The solubility of β-stabilizers in α-Ti is much lower than in β-Ti, and the theory also predicts that impurities, such as oxygen, nitrogen and or carbon, can change the energy barrier for the α→ω pathway [21] and can, consequently, alter its microstructure, and its surface energy and mechanical properties. The driving force for grain growth is the reduction in the free energy associated with the decrease in the GB area [22]. Grain growth takes place by diffusion with a high enough

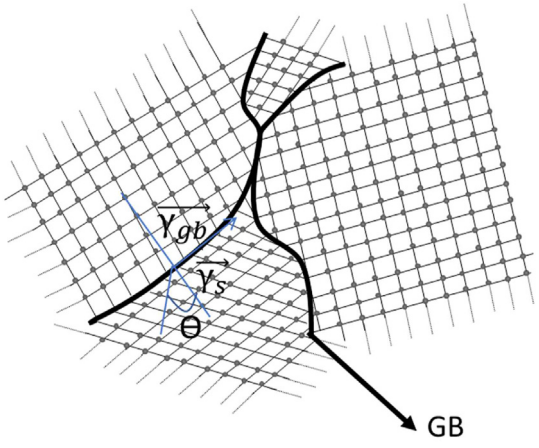

Fig. 1 – Schematic figure of grain boundaries and surface energies.

temperature and a long enough solution treatment time. The mechanism of the grain growth process includes normal grain growth and abnormal grain growth, or secondary recrystallization. The main studies about the grain growth mechanism have shown that grain growth kinetics can be analyzed by either measuring the average GS of the whole samples in the micrograph or using advanced measuring equipment and analysis techniques [23], as well as plastic deformation of β-Ti alloys to develop refined microstructures [24], microstructural evolution of β-Ti alloys during solution and aging treatment [25], corrosion and anti-bacterial properties [26], the acquisition of low elastic modulus beta-type Ti–Nb alloys by addition of alloy elements for antibacterial implant applications [27]. The aim of this work is to understand the mechanism of the β grain growth behavior related to β alloys element contents, and to provide experimental evidence for the role of an alloying element in Ti alloy design and its influence on surface and mechanical properties. The correlation of the alloy elements among free energy, contact angle and roughness of β-Ti alloys with a low modulus scarcely appears in the literature. Despite evidence for positive effects of high-surface energy associated with hydrophilic surfaces for improved cellular interactions, it is imperative to understand the influence of alloy elements on microstructure properties that orchestrate free energy. In the present study, as-cast β-Ti alloys with different β alloy amount (Ti-xNb, Ti-xNb-yZr, and Ti–Nb–Zr–Ta). The novelty of this work was to understand the increase or decrease of different surface and mechanical parameters based on Mo_{eq} values, once anyone reports about this correlation was found in the literature (see Fig. 1).

2. Materials and methods

2.1. Materials processing

The selection of the alloys was based on different alloy element content resulting as consequence on different phase stability (Ti–15Nb: majority α/α-prime + β, Ti–40Nb β stable, Ti–33Nb–33Zr: β metastable, Ti–40Nb–40Zr: β stable Ti–35Nb–7Zr–5Ta: β stable) at room temperature and also different chemical composition that could influence on their surface and mechanical properties. More specifically, at low β stabilizer element content on Ti microstructure, promote a formation of martensite α-prime phase that is identical to that of the equilibrium α phase or an orthorhombic martensite [28]. Increasing the β stabilizer element also adding neutral elements (e.g., Zr) can contribute to the stability of the β Ti alloys at room temperature [29]. Besides, correlate the β grain growth behavior related to β alloys element contents, to physical, surface and mechanical properties. A schematic of the mechanism of the grain growth of the specific alloys in this work is represented in Fig. 2.

An arc melting furnace with a non-consumable tungsten electrode on a water-cooled copper hearth (Edmund Bulher model D-72411) was used to melt ingots of β-Ti alloys Ti–15Nb (TN-15); Ti–40Nb (TN-40); Ti–33Nb–33Zr (TNZ-33); Ti–40Nb–40Zr (TNZ-40) and Ti–35Nb–7Zr–5Ta (TNZT) (wt.%) in an ultrahigh purity argon atmosphere. Before the melting process, raw materials were prepared by cutting them to the applicable sizes and subsequently weighing them according to the material balance calculation and loading them on the top of a copper crucible in the melting chamber. The melting process took place in a vacuum, which is achieved by pumping the chamber up to the vacuum condition (10^{-5} mbar) and subsequently draining it by argon so that the melting chamber is free of oxygen. Ingots were remelted 8 times to ensure process completion rather than improving their chemical homogeneity. For characterization purposes, 1-mm cuts were made in the cross-section of alloys using a high-speed cutter (Isomet 5000-buehler). Then they were subjected to conventional metallographic gridding and polishing up to mirror appearance with 0.25 μm diamond suspension, followed by 1 μm colloidal silica diluted with 10 vol.% hydrogen peroxide. Samples were cleaned with distilled water and ethyl alcohol/acetone for 1 h in an ultrasonic bath.

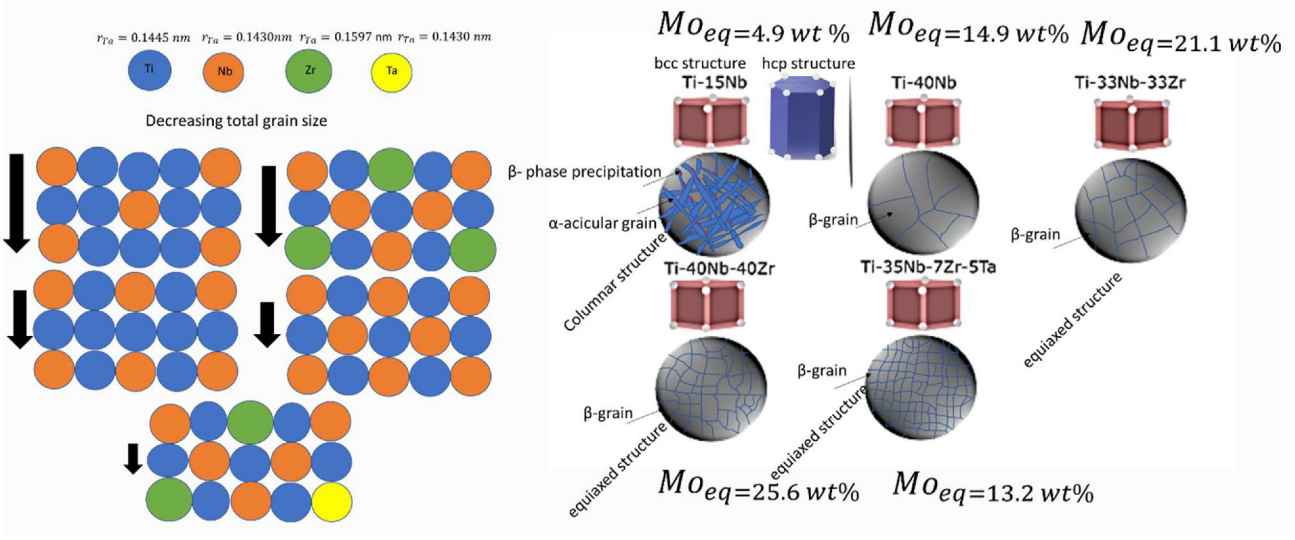

Fig. 2 – Schematic of the mechanism of the grain growth process of as-cast β-Ti alloys.

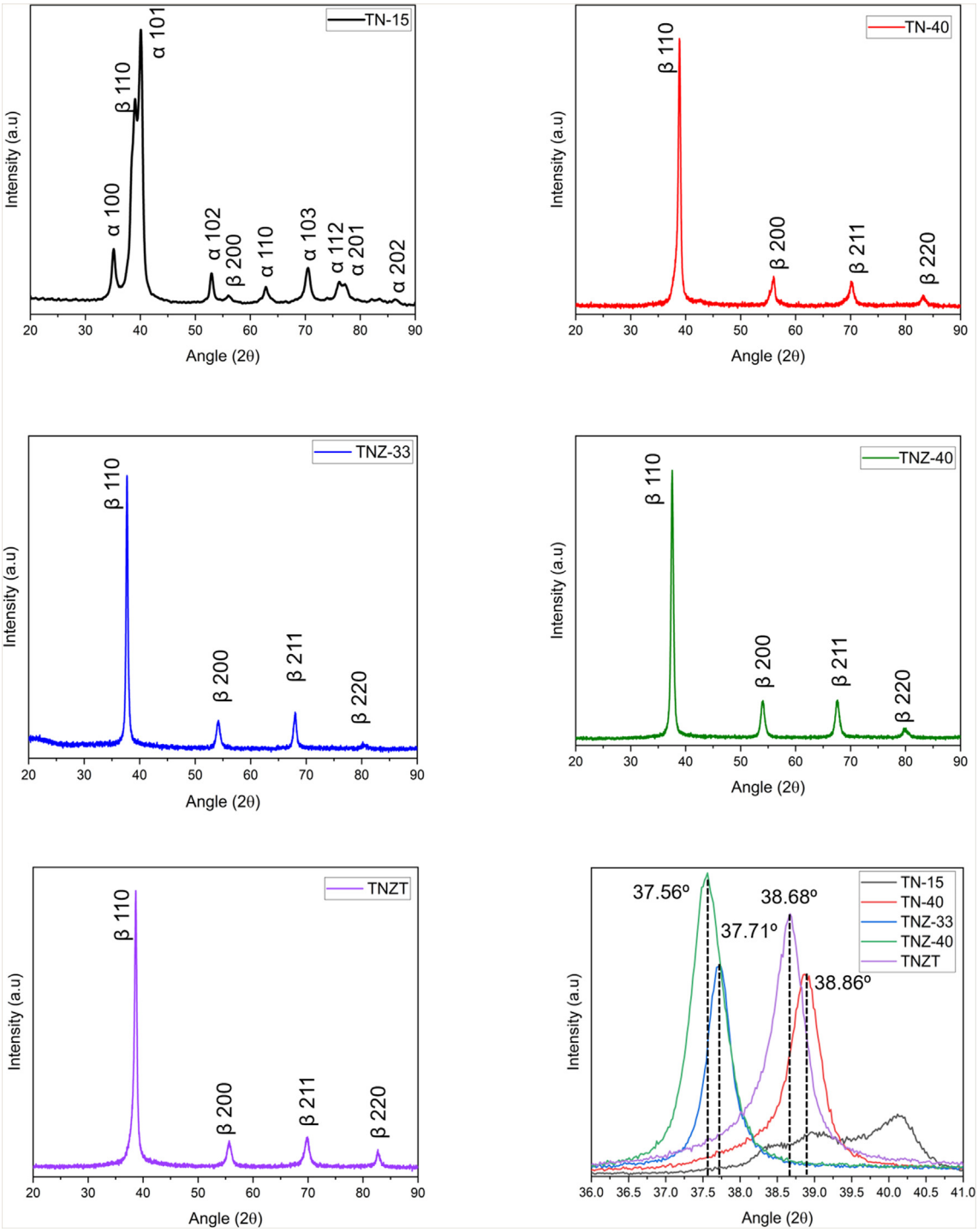

Fig. 3 – XRD profiles of the as-cast β-Ti alloys.

Table 1 – Structural parameters obtained by Rietveld refinement.

Material	sig	RWP	<D> (Å)	ε (rms)	a (Å)
TN-15	1.5	16	863 ± 14	$0.0123 \pm 3.99 \times 10^{-4}$	$3.30 \pm 10.56 \times 10^{-4}$
TNZT	1	10	180 ± 1	0.003731 ± 0.00098	$3.30 \pm 5.27 \times 10^{-4}$
TN-40	1.9	6	211 ± 2	0.0002 ± 0.0199	$3.32 \pm 6.98 \times 10^{-4}$
TNZ-33	1.5	10	354 ± 1	$0.0013 \pm 7.96 \times 10^{-5}$	$3.38 \pm 4.68 \times 10^{-4}$
TNZ-40	1	6	251 ± 2	$0.0056 \pm 4.91 \times 10^{-5}$	$3.40 \pm 3.53 \times 10^{-4}$

2.2. Microstructural characterization

To understand the influence of the different β-stabilizer elements on the GSs and GBs of alloys, an Olympus - BX41M-LED optical microscope, paired with the Infinity Capture application suite software, was used. For this purpose, they were previously etched with Kroll's (Water 92.82%, Nitric Acid 6.11%, Hydrofluoric Acid 1.07%) reagent. Samples were observed at magnifications 100x, 200x, 500x and 1000x. The identification and quantification of phases were performed by X-ray diffraction (Bruker - D8 Advance Eco) with Cu Kα radiation (λ = 0.15418 nm) at 40 kV and 25 mA, a step size of 0.02° and a scanning speed of 0.02° s^{-1}. Refinement of the structural parameters and the quantitative analysis of phases were carried out by the Material Analysis Using Diffraction (MAUD) software (version 2.94). Phases and diffraction planes were analyzed by comparing the d-space value of each peak of the diffraction pattern to those of the Inorganic Crystal Structure Database (ICSD). To more precisely characterize the microstructure, as with the grains and phase quantifications, electron backscattered diffraction (EBSD) with a scanning electron microscope (Zeiss-ULTRA 55 operating at 20 kV), equipped with an Aztec HKL Max System (Oxford Instruments Ltd.), was applied at an acceleration voltage of 20 kV and a 0.1 μm step size by selecting the two possible phases to be analyzed: bcc β-Ti (pdf-number: 5475) and hcp α-Ti (pdf-number: 253841).

2.3. Surface properties

2.3.1. Wettability and contact angle

Wettability is a chemical property that determines the ability of a liquid to spread over a material. In fact, it is also related to the surface tension of that material. Namely if that angle is less than 90° the material is hydrophilic whereas if it is more, it is hydrophobic. Moreover, surface tension is higher in cases where the material is hydrophobic. This surface tension is a characteristic value of the interaction between the surface of a condensed phase with the surrounding environment. However, this term refers to liquids. In the case of solids, it can be understood as the surface energy and is a decisive factor for the coating or adhesion capacity of a material, which is especially important in the biological environment. Furthermore, unlike surface tension, the surface free energy of a solid is referenced to any liquid, so when is high, the solid is usually easily wetted by any liquid. To estimate the surface energy values of solids, it is possible to do by measuring the contact angles with a DSA25S KRÜSS Drop Shape Analyzer which, using polar and non-polar test liquids, provides the values of these properties. The two contact liquids used were distilled water, to measure the dispersive component of the surface energy, and diiodomethane, to measure the polar one. This equipment has a specific software that with the Owens-Wendt-Rabel-Kälble (OWRK) method allows relating the contact angle (Θ) to the surface tension values (γ). In particular, this method distinguishes between two specific types of interactions, dispersive (γ_d) and polar (γ_p) surface tension. All these parameters are related according to the mathematical expressions given in Equations (4)–(6).

$$\gamma[\mathrm{mN/m}] = \gamma_d[\mathrm{mN/m}] + \gamma_p[\mathrm{mN/m}] \tag{4}$$

$$\gamma_{SL}[\mathrm{mN/m}] = \gamma_S[\mathrm{mN/m}] + \gamma_L[\mathrm{mN/m}] - 2\cdot(\gamma_{Ld}\cdot\gamma_{Sd})^{1/2} - 2\cdot\left(\gamma_{Lp}\cdot\gamma_{Sp}\right)^{1/2} \tag{5}$$

$$\gamma_S = \gamma_{LS} + \gamma_L\cdot\cos(\Theta[\mathrm{rad}]) \tag{6}$$

The contact angle technique was followed to determine the melted alloys' free surface energy. To evaluate the melted alloys' surface properties, samples were neither ground nor polished. Experiments were carried out at 37 °C. Three analyses were performed per sample. By means of white light interferometry (WLI) (Profilm3D- Filmetrics®), it was possible to take 3-dimensional profile roughness measurements of the surface samples according to ISO 9000.

2.4. Vickers microhardness and elastic modulus

Vickers microhardness values were obtained with a Shimadzu HMV - G20ST by applying 0.5 kgf for 15 s following ASTM-E384, with an average of 10 measurements. Elastic modulus, E, was

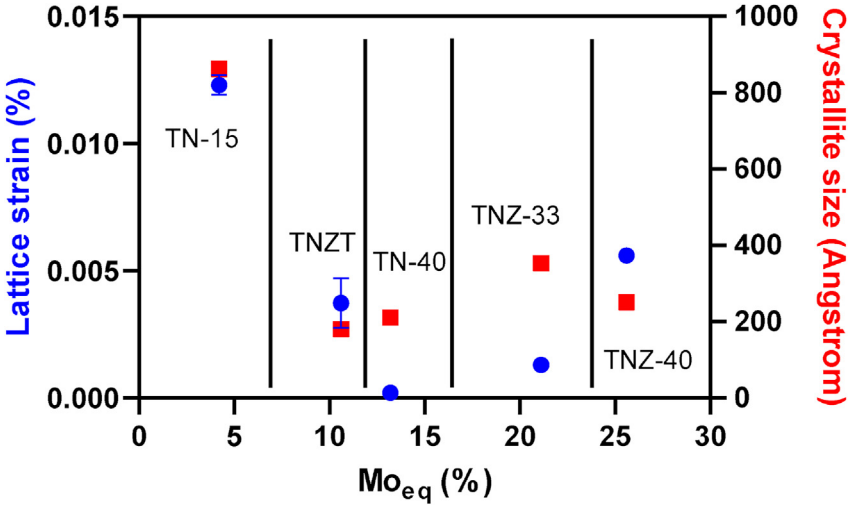

Fig. 4 – Structural parameters obtained by Rietveld refinement using the MAUD software.

evaluated by the impulse excitation technique (ATCP, Sonelastic) following ASTM E1876 - 15. Four measurements of each sample were taken.

2.5. *Oxygen content evaluation*

The oxygen concentration is an important factor that influences the microstructure and, consequently, the mechanical properties of Ti alloys. In this case, oxygen content was analyzed in all the samples with Leco RO400 equipment by applying the inert gas fusion principle using a free oxygen Ni basket inside a graphite crucible to release oxygen from samples according to ASTM-E1019.

3. Results and discussion

The influence of alloy element content on β Ti alloys during β phase formation is illustrated in Fig. 3, which indicates the XRD profile of the as-cast samples. The binary samples (Ti-xNb) showed a significant difference in the profile XRD, where it is possible to note phases α and β formation in the samples formed with 15 wt%, in accordance with the work of kuroda et al., 2020 [30] which differ from that of 40 wt%, and where only phase β is formed. Nb content over 35 wt% was capable of promoting the allotropic transformation of α-Ti → β-Ti. The ternary alloys (Ti–33Nb–33Zr, Ti–40Nb–40Zr) presented a

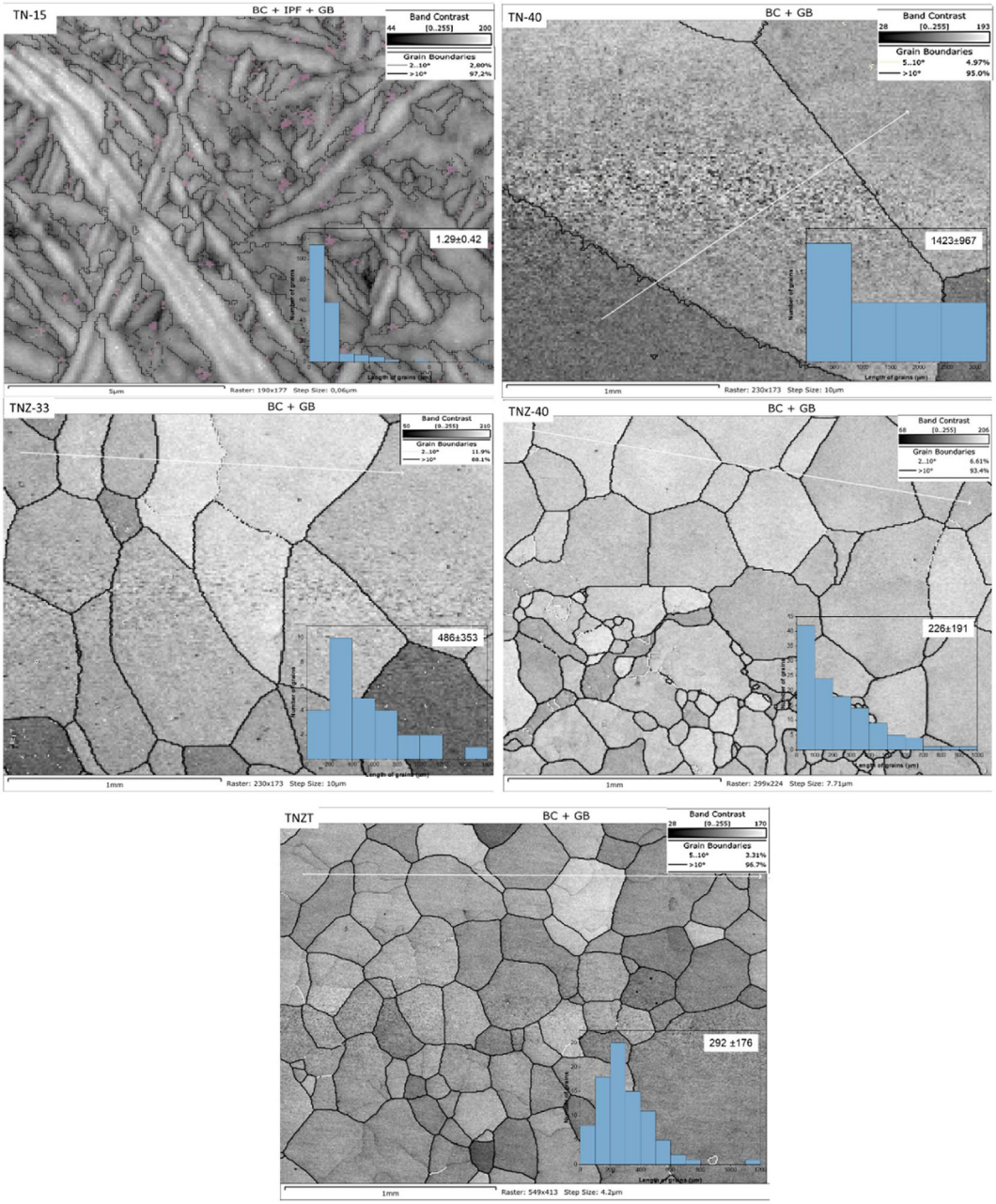

Fig. 5 – EBSD characterization of the as-cast β Ti-alloys using band contrast (BC) images. Distribution of grain size (um) by the EBSD technique of the as-cast β-Ti alloys. For this analysis, the same magnification (50x) was used for all the samples.

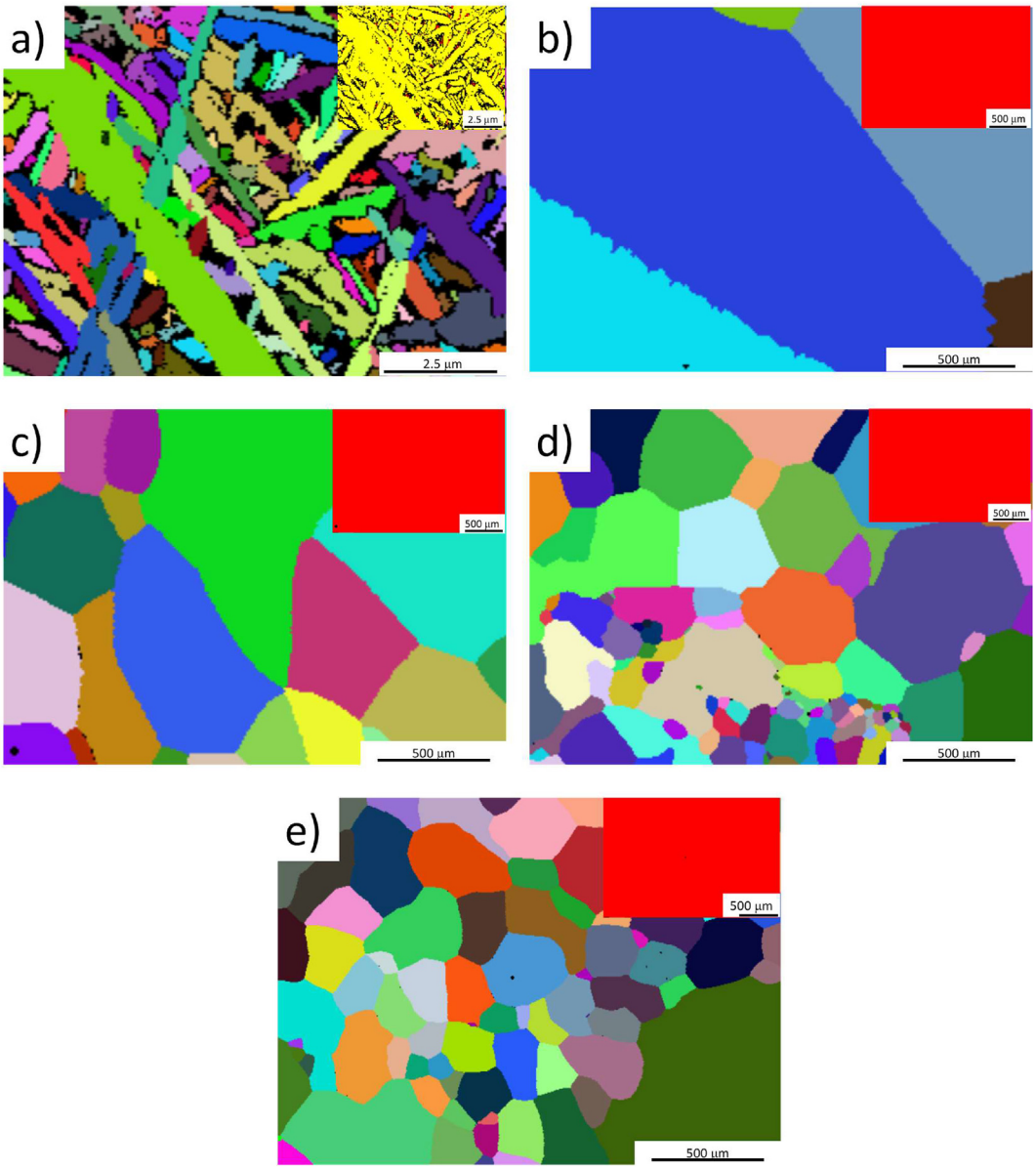

Fig. 6 – Grain map of the as-cast β-Ti alloys obtained by EBSD a) TN-25 alloy, b) TN-40 alloy, c) TNZ-33 alloy, d) TNZ-40 alloy and e) TNZT alloy and their respective EBSD micrograph comparing phases β and α, respectively denoted by red and yellow.

similarity in the profile XRD, with only a slight difference in the reflection peak represented by <220>. This difference can be related to the highest Nb and Zr contents in the Ti–40Nb–40Zr alloy. It is also possible to note that Zr promoted the displacement of the pattern for some low angles because of its small atomic radius compared to Ti [31,32], which indicates a change in the lattice parameter. To confirm the difference between the samples with different element contents in structural characteristics, Rietveld refinement was applied. The results are indicated in Table 1. Refinement quality was shown by the sigma and RWP parameters obtained during refinement, which denote a good fit once the sigma for all the samples was less than 2 and RWP went below 15.

Crystallite size, microstrain and cell parameter presented a significant difference based on the alloy element content in the β-Ti alloys. The crystallite size decreased when the Nb

Table 2 – Surface properties of the as-cast β-Ti alloys obtained by profilometry (roughness) and the sessile drop method, contact angle (Θ) and free energy (mN/m), compared with Mo equivalent.

Materials	Contact angle (Θ)	Free energy (mN/m)	Roughness (μm)	Mo_{eq} (wt %)
TN-15	55.1 ± 1.4	51.9 ± 5.1	1.3 ± 0.2	4.9
TNZT	58.3 ± 2.0	54.5 ± 1.6	1.9 ± 0.8	13.2
TN-40	52.4 ± 1.5	56.6 ± 2.8	3.0 ± 0.0	14.9
TNZ-33	44.1 ± 6	56.3 ± 2.5	2.6 ± 0.5	21.1
TNZ-40	60.2 ± 1.6	52.3 ± 1.5	2.0 ± 0.4	25.6

Table 3 – Physico-mechanical parameters obtained for as-cast β-Ti alloys.

Materials	Density, ρ (g/cm^3)	Microhardness, HV	Elastic Modulus, E (GPa)	Shear Modulus, G (GPa)	Mo_{eq} (wt%)
TN-15	4.08	264 ± 13	65 ± 1	38 ± 0.1	4.9
TNZT	5.74	163 ± 18	64 ± 3	24 ± 0.9	13.2
TN-40	5.22	198 ± 8	54 ± 1	19 ± 0.3	14.9
TNZ-33	5.27	211 ± 10	78 ± 1	33 ± 0.3	21.1
TNZ-40	6.25	232 ± 35	75 ± 1	30 ± 0.1	25.6

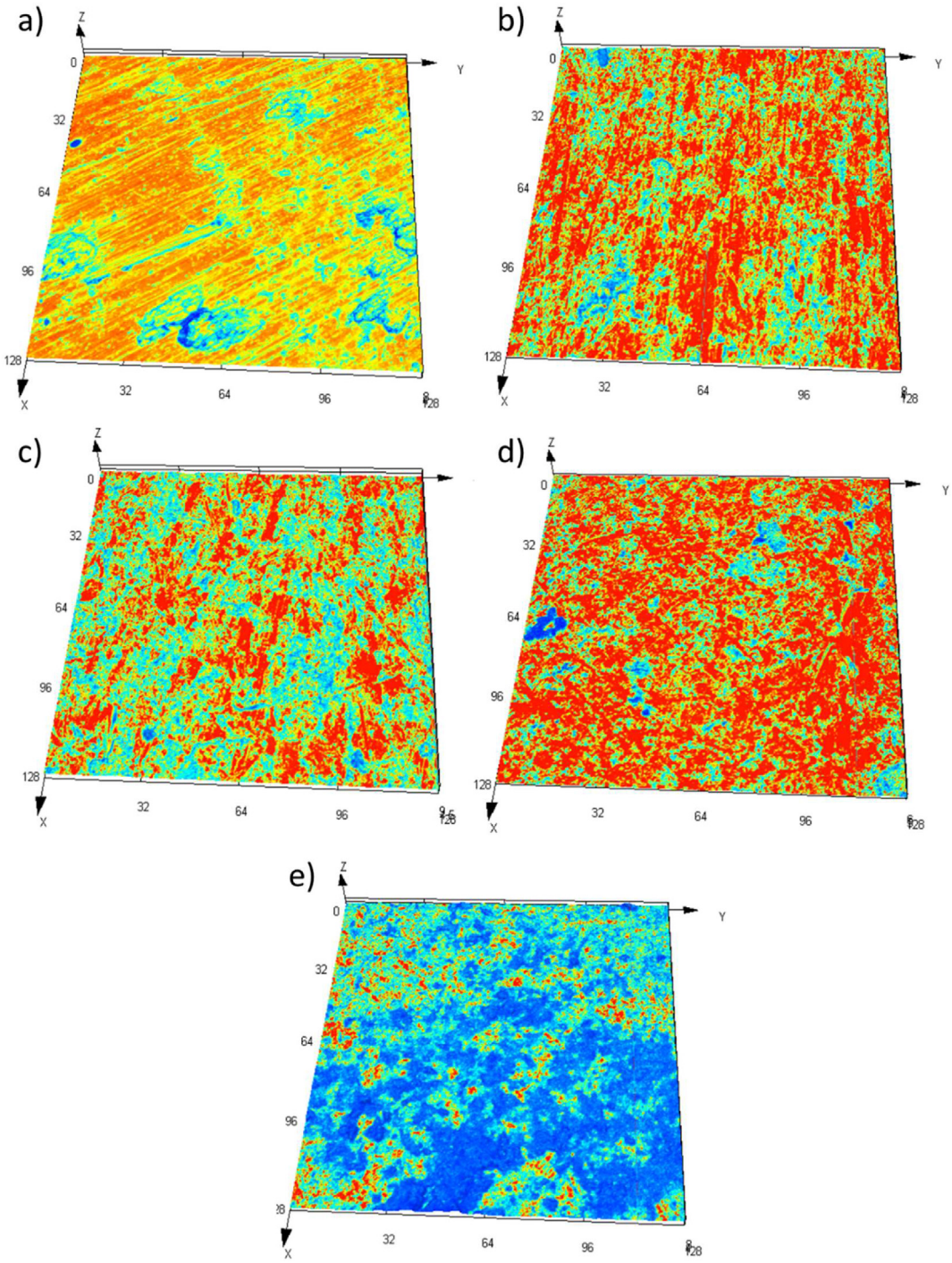

Fig. 7 – Roughness profile by confocal microscopy of as-cast surface Ti alloys after finished with # 600 mesh sandpaper.

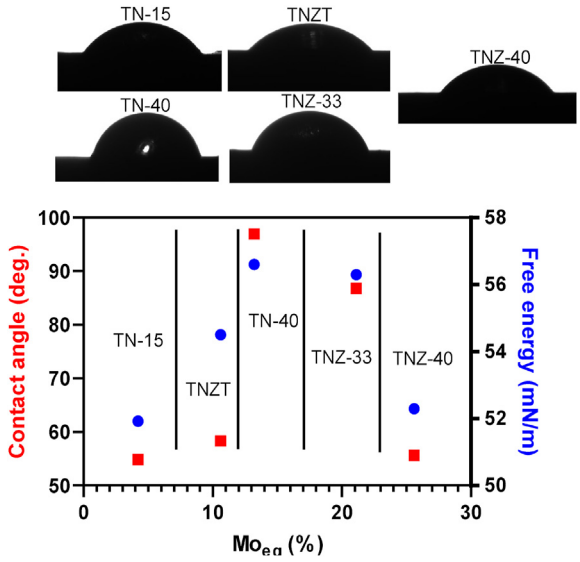

Fig. 8 – Wettability and free energy surface measured by the sessile drop method. For the free energy surface data, distilled water (as the polar agent) and Di-iodomethane (as the non polar agent) were used.

content of Ti–15Nb → Ti–40Nb increased, which suggests β phase stabilization. The ternary alloys presented a significantly decreasing crystallite size with variation in Zr content. As crystallite size is a structural coherence measure length, which may be strongly influenced by structural lattice distortions, it made the influence of Zr on increasing crystallite size once the atomic radius of Zr was larger than Ti quite clear. As the Nb, Zr and Ta ions are smaller than Ti, crystallite size decreased during replacement due to the lattice strain induced by size mismatch. The quaternary alloy had the smallest crystallite size compared to another alloys. The mechanism of decreasing crystallite size can be explained by the same replacement solid solution found in the ternary alloys. The microstrain displayed the same tendency in all the alloys once crystallite size decreased as the microstrain increased. A better understanding of the phase transformations peculiarities in Ti–xNb-(Zr,Ta) alloys can be gained by making purely geometrical comparisons of the lattices of the observed phases. The starting point of such discussion is to estimate changes in the lattice parameters of the different phases that occur due to variation in Nb and Zr contents. The lattice parameters increased with rising Nb and Zr contents, which was probably related to the larger radius of these atoms compared to that of Ti. However, the lattice parameter of the TNZT alloy was similar to the TN-15 alloy. These parameters will strongly influence the mechanical properties of the as-cast alloys herein studied, which is discussed later.

Table 4 – Oxygen content of the as-cast samples by a gas sensor analyzer.

β Ti Alloys	Oxygen (wt.%)
TN-15	0.195 ± 0.004
TNZT	0.044 ± 0.012
TN-40	0.126 ± 0.001
TNZ-33	0.101 ± 0.003
TNZ-40	0.114 ± 0.008

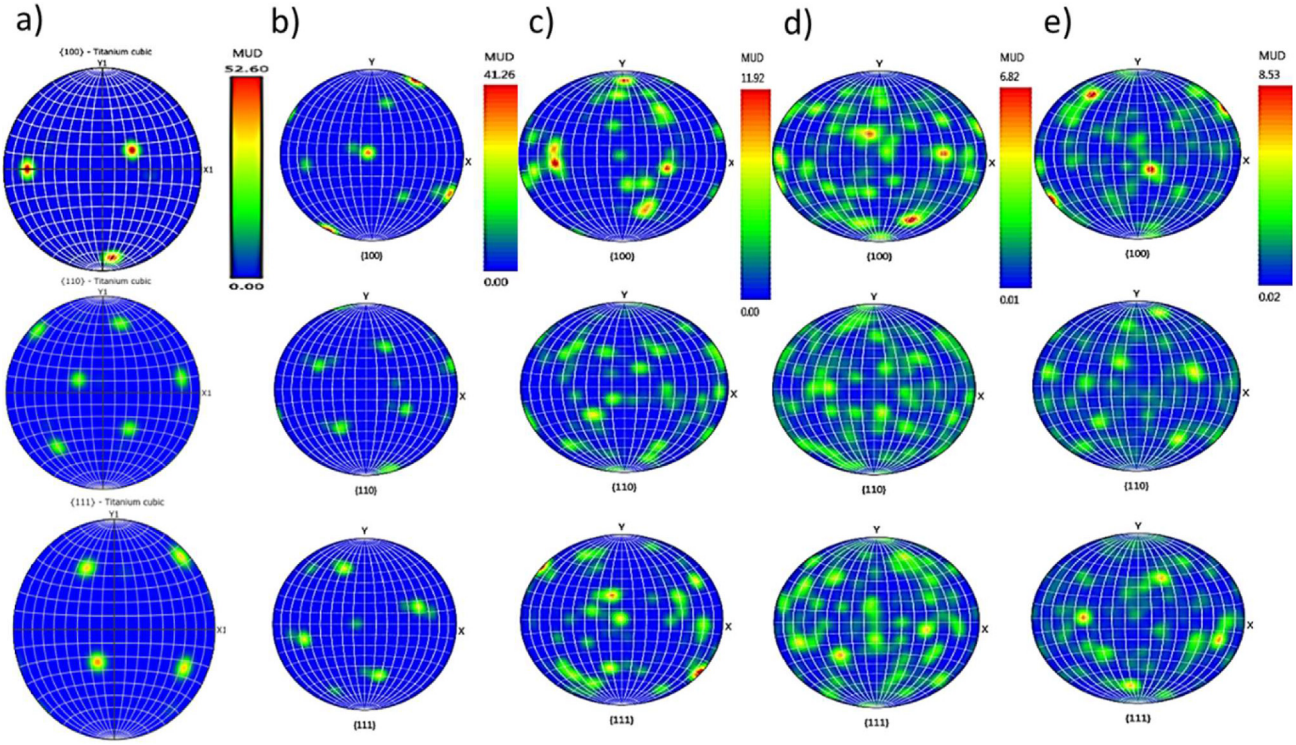

Fig. 9 – Texture evaluation using the pole figures represented by the {100}, {110} and {111} β families of the as-cast samples a) TN-15 b) TN-40 c) TNZ-33 d) TN-40 and e) TNZT.

Table 5 – Comparison of the influence of β stabilizer elements content on the cell parameters, elastic modulus and microhardness values of the as cast β-Ti alloys.

Materials	Cell Parameter (Å)	Elastic Modulus, E (GPa)	*Microhardness, HV*
TN-15	$3.30 \pm 10.56 \times 10^{-4}$	65 ± 1	264 ± 14
TNZT	$3.30 \pm 5.27 \times 10^{-4}$	64 ± 3	164 ± 18
TN-40	$3.32 \pm 6.98 \times 10^{-4}$	54 ± 1	197 ± 8
TNZ-33	$3.38 \pm 4.68 \times 10^{-4}$	78 ± 1	211 ± 11
TNZ-40	$3.40 \pm 3.53 \times 10^{-4}$	75 ± 1	232 ± 35

The crystallite size and microstrain of the as-cast β-Ti alloys correlated with Mo_{eq} (wt%) and are represented in Fig. 4. The Mo_{eq} (wt%) values increased to 13.20, and the lattice strain decreased and then started to increase. However, crystallite size presented more variation by decreasing to 10.60 of Mo_{eq}, and then increasing and decreasing again.

The typical grain structures of the as-cast β-Ti alloys are represented in Fig. 5. As shown, the TN-15 alloy is distinguished from the others by being formed by the combination of small elongated grains with ECD = 0.22 μm for β grains and 0.62 um for α grains. TN-40 mostly constitutes equiaxed large grains (ECD = 842 μm). The TNZ-33 and TNZ-40 alloys are formed by equiaxed grains, and TNZ-33 is more symmetric than TNZ-40 with ECD values of 334 μm and 155 μm. The TNZT alloy is constituted by smaller symmetric equiaxed grains than TNZ-33, with ECD = 208 um. The band contrast figures indicate that GS significantly decreases when adding Nb and Zr. Adding the β-stabilizing elements also results in grain refinement by changing the solidification pathway and the β-phase forming to enhance alloys' workability, as reported in the literature [33–36]. The GBs for all the samples are formed mainly by HAGB, and TNZT GB has the highest HAGB value.

The microstructural morphological characteristics of the as-cast β-Ti alloys are shown in Fig. 6a–e. The TN-15 alloy microstructure was heterogeneous, and millimetric equiaxed GSs were differentiated. Two phases in this system were found, and one of them formed mostly inside the acicular α grains (submicron β phases), as confirmed in Fig. 4. When increasing the β stabilizer content Nb to 40 wt %, GS visibly increased, with a change from its acicular morphology to an equiaxial one with more homogeneous distribution. In the ternary systems (Fig. 6c and d), a similarity was noted to the microstructure of both alloys. Equiaxed micrometric grains formed for both the TNZ-33 and TNZ-40 alloys. In the same way, the quaternary alloy TNZT (Fig. 6e) was formed by micrometric equiaxed β grains that were more homogeneous in size than the other alloys.

Table 2 indicates the surface parameters of the as-cast alloys. Al the surface samples were prepared equally using # 600

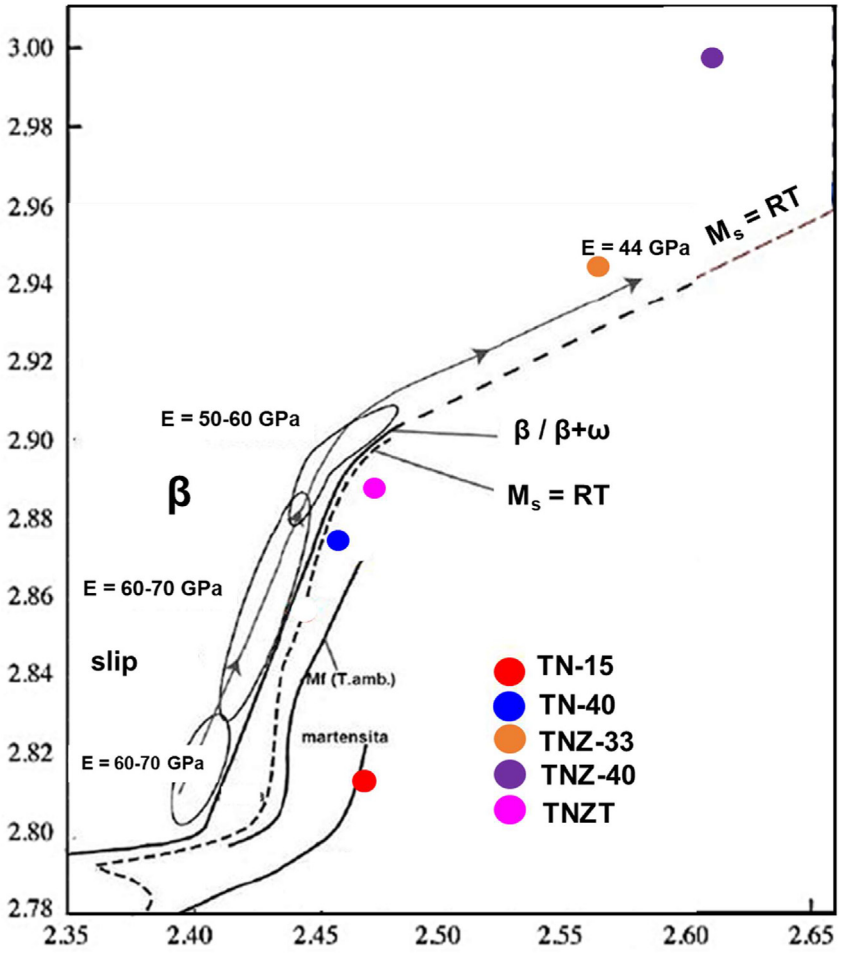

Fig. 10 – Bo x Md diagram of as-cast beta Ti alloys.

mesh sandpaper. The contact angles of the polar solvent under alloys' surface were above 90°, which means that all the surfaces presented good wettability for being applied as biomaterial. This is, in turn, suitable for the initial protein attachment [37]. The contact angle decreased and the alloy element content increased to TNZ-33. Then wettability decreased and the contact angle increased. Surface free energy fell within the of 51–56 mN/m range, with the minimum value in TN-15 and the maximum value in TN-40 and TNZ-40.

To evaluate the influence of topography on wettability and free energy, roughness was measured by a profilometer as can see on Table 3 and Fig. 7. Roughness decreased when increasing the alloy element, and is independent on wettability and free energy.

For the 13.20 Mo_{eq} (wt %) values, roughness increased and then started to decrease, which differs from the contact angle, which dropped to 21.12 of Mo_{eq} (wt%). All the surface samples were finished using sandpaper of the same granulometry (# 600 mesh) to remove the influence of surface morphology on the analyses. The protocol used to finish the samples was the same in the work of Ricci et al. [38]. It was clear that alloying elements content played significant roles in the roughness properties on the β-Ti alloys. To date, it has been demonstrated that surface roughness is related to the morphology properties of metallic materials, such as: pore size, pore geometry, number of pores and influence of using a different finishing mechanism. They all influence the topography of surfaces [39–41]. However, when the same finished process was used for all the samples in this work, a significant difference appeared between the alloys with a different Mo_{eq} or alloy element content. This finding demonstrates that roughness can be related to other surfaces parameters (i.e.: grain geometry, GS, GBs and free energy surface). According to the wettability of the as-cast samples, they can all be classified as hydrophilic once the contact angle is $\Theta < 90°$. Besides, the less the contact angle present, the more wettable the surface is. So according to this work, the wettability of the as-cast β-Ti alloys can be classified as: TNZ-33 > TN-40 > TN-15 > TNZT > TNZ-40. As samples' roughness varied between 1.3 and 3 microns, they can be classified as: TN-40 > TNZ −33 > TNZ-40 > TNZT > TN-15.

Fig. 8 represents the relation between the free energy surface and the contact angle with the Mo_{eq} (%) of each sample. Both free energy surface and wettability are intrinsically related to samples' microstructure and surface properties. Once all the samples presented the same finishing, surface properties were the same for them all. This means that the difference between them can be correlated with GS, GBs and alloy element content. It was noteworthy that TN-15, with a low Mo_{eq} (wt%), had a close contact angle and free energy with TNZ-40, which presented high Mo_{eq} (wt%). From these results, we can note that the influence of Mo_{eq} (wt%) displayed the opposite behavior on both the contact angle and free energy surface of the as-cast samples. When increasing the Mo_{eq} (wt %) values to 13.2 wt%, the free energy increase then started to lower, unlike what occurred with the contact angle, which started lowering to 21.12 Mo_{eq} (wt%) and then increasing. The results in Figs. 5 and 6 were corroborated once the contact angle and free energy surface became inversely proportional parameters.

As shown in Fig. 9, the inverse pole figures with specific orientation parallel to the x-y surface of the β phase are adopted to indicate texture characteristic information. The {100} pole figure exhibits higher density points compared to the {110-011} pole figures, which indicate the formation of several textures. The multiples of the uniform distribution (MUD) of the measured β phase are also represented with the specific dataset of the pole figures. MUD intensity was greater in the TN-15 alloy then decreased to TNZ-40 and slightly increased in TNZT. From these results, we can conclude that the α-phase of TN-15 exhibits a clear crystallographic orientation with the maximum MUD value of 52.60 (a measure of the crystallographic preferred orientation strength, followed by the β-phase of TN-40 with the maximum MUD value of 41.2). More specifically, with Nb less content many crystals are tilted ~ 45° about the columnar or growth direction of the α phase. However, when increasing the amount of Nb and adding Zr, the MUD value drastically drops with the resulting equiaxed prior-β grain structure, and no other preferred texture is detected. These observations are consistent with the understanding that an equiaxed grain structure has no preferred crystallographic texture.

The influence of the β stabilizer elements on mechanical properties was evaluated by microhardness and impulse excitation techniques. They are represented in Table 3. Both microhardness and the elastic modulus present the same tendency when increasing alloy element content and can be correlated with Mo_{eq} (%) and microstructure. For the samples with 15 wt % of Nb (TN-15), microhardness and elastic properties are higher. When increasing the Nb addition for 40 wt % (TN-40), the reduction in mechanical properties by increasing the β phase content becomes clear also in accordance to Santos et al., 2021 [42].

The main difference found between these two compositions is the presence of a harder phase (α-Ti) and Mo_{eq} %. The TN-15 samples were formed by a heterogeneous microstructure (α + β phases), with an average GS of 1.29 μm and an Mo_{eq} of 4.95 wt %. For the TN-40 alloy, the microstructure was more homogeneously formed totally for all the β -Ti grains (1423 μm) which was less harder compared to α-Ti, and with an Mo_{eq} of 13.2 wt%. These characteristics determined these alloys' mechanical properties. By introducing Zr as a neutral element, mechanical properties increased, except for the quaternary system, namely TNZT, with a similarity to the mechanical properties compared to TN-15 once the Mo_{eq} values of both systems were quite close. As these samples were formed by β grains, it can be excluded in the phase content as an influence

Table 6 – Bo, Md (B_o and M_d should be underwritten as described in figure 10) and Moeq (Mo_{eq} is also should be underwritten as described troughout the article.) values obtained from Eqs.(2) and (3) of as-cast beta Ti alloys.

Materials	B_o	M_d	Mo_{eq}
TN-15	2.816	2.445	4.9
TNZT	2.884	2.467	13.2
TN-40	2.869	2.441	14.9
TNZ-33	2.942	2.565	21.1
TNZ-40	2.994	2.605	25.6

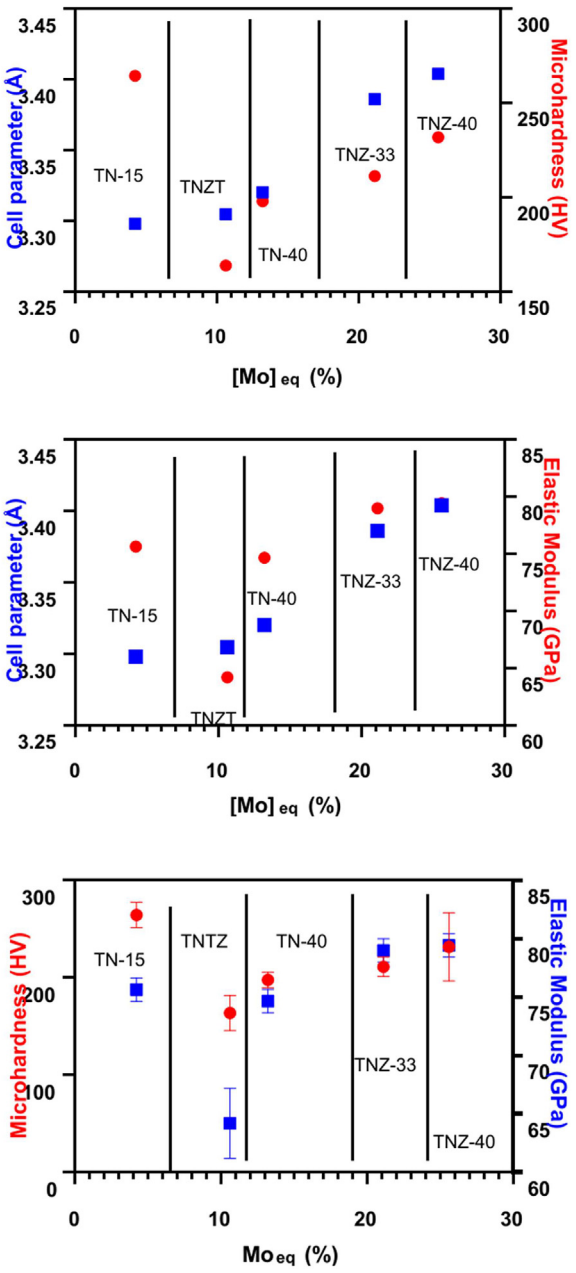

Fig. 11 – Relation among the elastic modulus, microhardness and cell parameter a_β of the as-cast β-Ti alloys.

of the mechanical parameter. The main difference is the GS distribution and texture characteristics, which decreased while adding Zr.

As previously discussed, variation in the lattice parameter can indicate an increase or decrease in the mechanical properties of a given alloy. In this case, the lattice parameters of the bcc phase (a_β) are indicated together with the microhardness and elastic modulus values of the alloys obtained by casting. The alloys with higher a_β values (TNZ-33 and TNZ-40) obtained higher values for hardness and elastic modulus, which corroborated the previously discussed data. Unlike the TN-15 alloy, with a heterogeneous acicular microstructure formed by the α+β phases, microhardness was higher than in all the other alloys, even with a lower lattice parameter. One of the possibilities for this increase is the presence of not only the hardening phase (phase α), but also of higher oxygen content compared to other materials (Table 4). According to Liu and Welsch, oxygen has extensive solubility in the α and β phases before forming oxide phases, and it is known as a strong α-stabilizing element. Dissolved oxygen in the α and β phases causes hardening from interstitial solid solution to strengthen and reduce ductility [43], which can be explained by the obtained results. In general, all the alloys of different systems indicated low interstitial oxygen content, which is in accordance with ASTM E1409-13 for applications as a metallic biomaterial (see Table 5).

According to the introduction of this work, the electronic Bo-Md maps can be used to predict the deformation mechanism occurring in a specific alloy composition, and the as-cast alloys studied in this work can be found in Fig. 10 and the values of B_o and M_d can be found in Table 6. The area between the Ms and Md lines corresponds to the occurrence of the stress-induced α″ martensitic phase transformation or SIM transformation. The Ms and Md correspond to the martensite start temperature and the minimum temperature above which β is stable and does not transform to martensite by deformation, respectively. The critical resolved shear stress (CRSS) for SIM is expected to increase on going from the Ms line toward the Md line and the SIM transformation will occur most readily near the Ms line. Mechanical twinning is expected to be the dominant deformation mechanism between the Md line and the borderline between the slip and twinning regions. It can be supposed that in the transition regions, the deformation mechanisms, two or three deformation mechanisms may occur in combination. Hence, to obtain different combinations of deformation mechanisms, the designed alloy should be targeted to locate close to the Ms, Md and Slip/Twin lines.

The correlation of the lattice parameter with microhardness and the elastic modulus according to the % of Mo_{eq} is shown in Fig. 11. It depicts how both microhardness and the elastic modulus vary in the same way for the lattice parameter and Mo_{eq} values. The same variation appears when comparing the microhardness and elastic modulus values according to % Mo_{eq}.

4. Conclusions

The respective Ti–15Nb (TN-15), Ti–40Nb (TN-40), Ti–33Nb–33Zr (TNZ-33), Ti–40Nb–40Zr (TNZ40) and Ti–35Nb–7Zr–5Ta (TNZT) alloys were fabricated by casting. Their microstructure, surface and mechanical properties were studied and correlated for biomedical field applications. The main conclusions are as follows.

- β-Ti alloys studied resulted in bcc β-Ti phase equiaxed grains in the range of hundreds of microns, except from the as-cast TN-15 alloy, which can be characterized as mainly acicular α′ phase (hcp) ranging from micro-to sub-micrometric size and a remaining bcc β-Ti phase.
- Increasing addition of Nb combined with Zr addition influences not only the values of the β-phase lattice parameter, but also crystallite size and lattice strain.

- Grain size of the stable β-Ti alloys decreases with increasing adding of Nb combined with Zr addition (replacing Ti), refining microstructure of the alloy in the order: TN-40 > TNZ-33>TNZT > TNZ40 and resulting in lower contact angle (increased wettability) of TNZ40 with smaller grain size.
- The lower Nb content of many crystals is tilted ~ 45° about the columnar or the growth direction of the α phase (TN-15). By increasing the amount of Nb or adding Zr, the MUD value drastically lowers, and the resulting equiaxed prior-β grain structure, and for the others a isotropy is detected
- Elastic and shear moduli, and microhardness decreased to Mo_{eq} 14.9 wt % and then their properties significantly increase, except for TN-15 alloy, which is formed mainly by the α′ phase with higher oxygen content
- Both the elastic modulus and microhardness follow the same tendency compared to the Mo_{eq} values according to cell parameter of the β phase (a_{β})

Declaration of Competing Interest

The authors declare that they have no known competing financial interests or personal relationships that could have appeared to influence the work reported in this paper.

Acknowledgment

This study was financed partly by the Coordenação de Aperfeiçoamento de Pessoal de Nível Superior of Brazil (CAPES), Finance Code 001, and Ph.D. grant # 88887.371759/2019-00 (R.F.M.S.). The authors wish to thank Brazilian agencies: CNPq Universal Project #422015/2018-0 (C.R.M.A.); FAPESP (São Paulo Research Foundation) for financial support through "Projeto Temático" # 2018/18293-8, *post doc* Grant # 2021/03865-9 (M.C.R.), PhD Scholarship 2021/11537-1 (A.L.V) and funding from Spanish Ministerio de Ciencia, innovación y Universidades with project RTI2018-097810-B-I00, and the European Commission via FEDER funds.

REFERENCES

[1] Saud SN, Hosseinian RS, Bakhsheshi-Rad HR, Yaghoubidoust F, Iqbal N, Hamzah E, et al. Corrosion and bioactivity performance of graphene oxide coating on Ti\\Nb shape memory alloys in simulated body fluid. Mater Sci Eng C 2016;68:687–94. https://doi.org/10.1016/j.msec.2016.06.048.

[2] Hamlet S, Alfarsi M, George R, Ivanovski S. The effect of hydrophilic titanium surface modification on macrophage inflam-matory cytokine gene expression. Clin Oral Implants Res 2012;23:584–90.

[3] Wang T, Bai J, Lu M, Huang C, Geng D, Chen G, et al. Engineering immunomodulatory and osteoinductive implant surfaces via mussel adhesion-mediated ion coordination and molecular clicking. Nat Commun 2022;13:160. https://doi.org/10.1038/s41467-021-27816-1.

[4] Hallab NJ, Bundy KJ, O'Connor K, Moses RL, Jacobs JJ. Evaluation of metallic and polymeric biomaterial surface energy and surface roughness characteristics for directed cell adhesion. Tissue Eng 2001;7:55–71. https://doi.org/10.1089/107632700300003297.

[5] Cai Shuxiang, Wu Chuanxiang, Yang Wenguang, Liang Wenfeng, Yu Haibo, Liu Lianqing. Recent advance in surface modification for regulating cell adhesion and behaviors. Nanotechnol Rev 2020;9:971–89. https://doi.org/10.1515/ntrev-2020-0076.

[6] Khorashadizade F, Abazari S, Rajabi M, Bakhsheshi-Rad HR, Ismail AF, Sharif S, et al. Overview of magnesium-ceramic composites: mechanical, corrosion and biological properties. J Mater Sci Technol 2021;15:6034–66. https://doi.org/10.1016/j.jmrt.2021.10.141.

[7] Gepreel MA, Niinomi M. Biocompatibility of Ti-alloys for long-term implantation. J Mech Behav Biomed Mater 2013;8:407–15.

[8] Abazari S, Shamsipur A, Bakhsheshi-Rad HR, Keshavarz M, Kehtari M, Ramakrishna S, et al. MgO-incorporated carbon nanotubes-reinforced Mg-based composites to improve mechanical, corrosion, and biological properties targeting biomedical applications. J Mater Sci Technol 2022;20:976–90. https://doi.org/10.1016/j.jmrt.2021.10.141.

[9] Rohrer GS. Grain boundary energy anisotropy: a review. J Mater Sci 2011;46:5881–95.

[10] Introduction to grains, phases, and interfaces—an interpretation of microstructure. Smith CS. Trans AIMME 1948;175:15–51. 175:15.

[11] Dillon SJ, Rohrer GS. Mechanism for the development of anisotropic grain boundary character distributions during normal grain growth. Acta Mater 2009;57:1–7. https://doi.org/10.1016/j.actamat.2008.08.062.

[12] Rohrer GS, Saylor DM, El Dasher B, Adams BL, Rollett AD, Wynblatt P. The distribution of internal interfaces in Polycrystals. Z Metallkd: international journal of materials research and advanced techniques 2004;95:197.

[13] Usikov MP, Zilberstein VA. The orientation relationship between the α- and ω- phases of titanium and zirconium. Phys. Status Solidi (A) Appl. Mater. Sci. 1973;19:53–8. https://doi.org/10.1002/pssa.2210190103.

[14] Feng B, Levitas VI, Kamrani M. Coupled strain-induced alpha to omega phase transformation and plastic flow in zirconium under high pressure torsion in a rotational diamond anvil cell. Mater Sci Eng 2018;731:623–33. https://doi.org/10.1016/j.msea.2018.06.061.

[15] Kuroda PAB, Quadros FdF, Nascimento MV, Grandini CR. Development and characterization of new Ti-25Ta-Zr alloys for biomedical applications. Mater Sci Forum 2021;1016:137–44. https://doi.org/10.4028/www.scientific.net/MSF.1016.137.

[16] Zhang J, Zhao Y, Pantea C, Qian J, Rigg P, Hixson R, et al. Experimental constraints on the phase diagram of elemental zirconium. J Phys Chem Solid 2005;66:1213–9.

[17] Boyer R, Welsch G, Collings EW. Materials properties handbook: titanium alloys. 4th ed. Ohio: ASM International; 1994.

[18] Leyens C, Peters M. Titanium and titanium alloys. Fundamentals and applications. 1st ed. Weinheim: WILEY-VCH Verlag GmbH & Co.; 2003.

[19] Hennig R, Trinkle DR, Bouchet J, Srinivasan SG, Albers RC, Wilkins JW. Impurities block the α to ω martensitic transformation in titanium. Nat Mater 2005;4:129–33. https://doi.org/10.1038/nmat1292.

[20] Morinaga M, Yukawa H. Alloy design with the aid of molecular orbital method. Bull Mater Sci 1997;20:805–15.

[21] Abdel-Hady M, Hinishita K, Morinaga M. General approach to phase stability and elastic properties of β-type Ti-alloys. Scripta Mater 2006;55:447–80.

[22] Gil FJ, Planell JA. Behaviour of normal grain growth kinetics in single phase titanium and titanium alloys. Mater Sci Eng 2000;283:17–24. https://doi.org/10.1016/S0921-5093(00)00731-0.
[23] Kuroda PAB, da Silva LM, Sousa KdSJ, Donato TAG, Grandini CR. Preparation, structural, microstructural, mechanical, and cytotoxic characterization of Ti-15Nb alloy for biomedical applications. Artif Organs 2020;44:811–7. https://doi.org/10.1111/aor.13624.
[24] Chen W, Li O, Zhou L, Li C, Qiu W, Chen J, et al. Limit of cold deformation in a near β-Ti alloy: role of α′ phases on the failure of β phase during cold rolling. J Mater Res Technol 2022;20:2385–93. https://doi.org/10.1016/j.jmrt.2022.07.192.
[25] Qi P, Li B, Wei W, Chen J, Wang T, Huang H, et al. Microstructural evolution and mechanical properties of a novel biomedical Ti–6Zr–4Fe alloy during solution and aging treatment. J Mater Res Technol 2022;21:429–37. https://doi.org/10.1016/j.jmrt.2022.09.063.
[26] Zhao Z, Xu W, Xin H, Yu F. Microstructure, corrosion and anti-bacterial investigation of novel Ti-xNb-yCu alloy for biomedical implant application. J Mater Res Technol 2022;18:5212–25. https://doi.org/10.1016/j.jmrt.2022.04.158.
[27] Alberta LA, Vishnu J, Hariharan A, Pilz S, Gebert A, Calin M. Novel low modulus beta-type Ti–Nb alloys by gallium and copper minor additions for antibacterial implant applications. J Mater Res Technol 2022;20:3306–22. https://doi.org/10.1016/j.jmrt.2022.08.111.
[28] Zheng Y, Banerjee R, Wang Y, Fraser H, Banerjee D. Pathways to titanium martensite. Trans Indian Inst Met 2022;75:1051–68. https://doi.org/10.1007/s12666-022-02559-9.
[29] Yang J, Baatarsukh M, Bae J, Huh S, Jeong H, Choi B, et al. Phase stability and properties of Ti-Nb-Zr thin films and their dependence on Zr addition. Materials 2018;11:1361. https://doi.org/10.3390/ma11081361.
[30] Gonzalez ED, Fukumasu NK, Afonso CRM, Nascente PAP. Impact of Zr content on the nanostructure, mechanical, and tribological behaviors of β-Ti-Nb-Zr ternary alloy coatings. Thin Solid Films 2021;721:138565. https://doi.org/10.1016/j.tsf.2021.138565.
[31] Zhou Y, Li Y, Yang X, Cui Z, Zhu S. Influence of Zr content on phase transformation, microstructure and mechanical properties of $Ti_{75-x}Nb_{25}Zr_x$ (x=0-6) alloys. J Alloys Compd 2009;468(1–2):628–6320. https://doi.org/10.1016/j.jallcom.2009.07.006.
[32] Chen Y, Li J, Tang B, Kou H, Xue X, Cui Y. Texture evolution and dynamic recrystallization in beta titanium alloy during hot-rolling process. J Alloys Compd 2015;618:146–52.
[33] Ferrandini PL, Cardoso FF, Souza SA, Afonso CRM, Caram R. Aging response of the Ti-33Nb-7Zr-5Ta and Ti-35Nb-7Ta alloys. J Alloys Compd 2007;433:207–10. https://doi.org/10.1016/j.jallcom.2006.06.094.
[34] Sheremetyev V, Kudryashova A, Cheverikin V, Korotitskiy A, Galkin S, Prokoshkin S, et al. Hot radial shear rolling and rotary forging of metastable beta Ti-18Zr-14Nb (at%.) alloy for bone implants: microstructure, texture and functional properties. J Alloys Compd 2019;800:320–60. https://doi.org/10.1016/j.jallcom.2019.06.041.
[35] Gonzalez ED, Afonso CRM, Nascente PAP. Influence of Nb content on the structure, morphology, nanostructure, and properties of Titanium-Niobium magnetron sputter deposited coatings for biomedical applications. Surf Coat Technol 2017;326:424–8. https://doi.org/10.1016/j.surfcoat.2017.03.015.
[36] Vlcak P, Fojt J, Koller J, Drahokoupil J, Smola V. Surface pre-treatments of Ti-Nb-Zr-Ta beta titanium alloy: the effect of chemical, electrochemical and ion sputter etching on morphology, residual stress, corrosion stability and the MG-63 cell response. Results Phys 2021;28:104613. https://doi.org/10.1016/j.rinp.2021.104613.
[37] Ricci VP, Santos RFM, Asato GH, Roche V, Jorge Junior AM, Afonso CRM. Assessment of anodization conditions and annealing temperature on the microstructure, elastic modulus, and wettability of β-Ti40Nb alloy. Thin Solid Films 2021;737:138949. https://doi.org/10.1016/j.tsf.2021.138949.
[38] Jemat A, Ghazali MJ, Razali M, Otsuka Y. Effects of surface treatment on titanium alloys substrate by Acid etching for dental implant. Mater Sci Forum 2015;819:347–52. https://doi.org/10.4028/www.scientific.net/MSF.819.347.
[39] Afonso CRM, Amigó AM, Stolyarov Gunderov D, Amigó V. From porous to dense nanostructured Beta-Ti alloys through high-pressure torsion. Sci Rep 2017;13618. https://doi.org/10.1038/s41598-017-13074-z.
[40] Wandra R, Prakash C, Singh S. Investigation on surface roughness and hardness of β-Ti alloy by ball burnishing assisted electrical discharge cladding for bio-medical applications. Mater Today Proc 2022;50:848–54. https://doi.org/10.1016/j.matpr.2021.06.075.
[41] Lu J-W, Zhao Y-Q, Ge P, Niu H-Z. Microstructure and beta grain growth behavior of Ti–Mo alloys solution treated. Mater Char 2013;84:105–11. https://doi:10.1016/j.matchar.2013.07.014.
[42] Santos RFM, Ricci VP, Afonso CRM. Influence of swaging on microstructure, elastic modulus and Vickers microhardness of beta Ti-40Nb alloy for implants. J Mater Eng Perform 2021;30:3363–9. https://doi.org/10.1007/s11665-021-05706-3.
[43] Liu Z, Welsch G. Effects of oxygen and heat treatment on the mechanical properties of alpha and beta titanium alloys. Metall Mater Trans 1988;19:527–42. https://doi.org/10.1007/BF02649267.